TENTH AUSTRALASIAN FLUID MECHANICS
CONFERENCE - UNIVERSITY OF MELBOURNE
11-15 DECEMBER 1989

NEAR-FIELD STRUCTURES IN THREE-DIMENSIONAL SPATIALLY-DEVELOPING WAKES

Jeffrey C. BUELL[1] and Nagi N. MANSOUR[2]

[1]Center for Turbulence Research, NASA Ames Research Center
Moffett Field, CA 94035, USA

[2]NASA Ames Research Center
Moffett Field, CA 94035, USA

ABSTRACT

The effects of three-dimensional perturbations on a spatially-developing plane Gaussian wake are studied and quantified using a new numerical code. Results are presented for a relatively simple case since it appears that no 3-D spatially-developing simulations of plane wakes have been performed in the past. The inlet perturbation consists of a 2-D time-periodic forcing plus a spanwise-periodic array of steady streamwise vortices. The distortion of the 2-D vortices caused by the streamwise vortices will be discussed. The vorticity fields are compared to passive scalar fields which simulate the injection of smoke or low heat into the wake.

1. INTRODUCTION

In this paper we examine the effects of three-dimensional (3-D) perturbations on a spatially-developing plane Gaussian wake at a moderate Reynolds number. Very few 3-D simulations of wakes have been performed in the past. Riley & Metcalfe (1980) performed a direct numerical simulation of the temporally-developing turbulent wake of an axisymmetric body using experimental data for the initial conditions. Although the mesh was coarse, low-order statistics compared well with the experiments. Meiburg & Lasheras (1988) reported results from wake experiments with different types of spanwise forcing and computed the flow using inviscid vortex dynamics calculations. It is difficult to use the latter to study small-scale details of free-shear flows, but they were able to reproduce the large-scale features of the experiments. More recently, Chen *et al.* (1989) performed well-resolved simulations of a compressible plane wake. Their main goal was to determine the effect of Mach number on the development of the wake, but they also described the development of 3-D structures which should be similar to the incompressible case.

In this work we present results for a relatively simple case where two different kinds of perturbations are added to a Gaussian mean inflow profile. The first is a two-dimensional (2-D) time-periodic forcing where the profiles for u (the streamwise velocity) and v (vertical velocity) are the eigenfunctions of the corresponding Rayleigh equations. Any frequency near the most amplified one produces the classical Kármán vortex street. The second kind of perturbation is a spanwise-periodic array of counter-rotating streamwise vortices. These are assumed to be steady as they might be in a wind tunnel with small nonuniformities in the last screen. As in the mixing layer and other shear flows, the streamwise vortices (usually referred to as *ribs*) are amplified by the strain field of the 2-D spanwise vortices (*rollers*). When the ribs become sufficiently strong, they distort the rollers through advection and strain effects. These effects will be contrasted with a 2-D simulation *sans* ribs. In addition, a passive scalar with a Gaussian profile is introduced at the inflow. It is often assumed in the experimental literature that smoke or heat introduced in the wake will follow the vorticity. The degree to which this is true will be tested in both the 2-D and 3-D simulations.

2. NUMERICAL METHOD

In this section we briefly describe a new algorithm for approximately solving incompressible spatially-developing free-shear problems on a domain that is infinite in the vertical (y) direction and finite in the streamwise (x) and spanwise (z) directions. The numerical method is analyzed in more detail elsewhere (Buell 1989).

Using the curl operator, the 3-D Navier-Stokes equations are reduced to equations for the streamwise velocity u and vorticity ω_1 ("fourth-order form"). These equations are advanced in time explicitly using a compact third-order Runge-Kutta scheme (Wray 1989). Since the Laplacian is contained in the time-derivative term, a Poisson equation must be solved for u during each substep. The dependent variables are expanded in either cosine or sine series in a mapped vertical coordinate ζ (where $y = -\beta\cot(\pi\zeta)$ maps $[-\infty,\infty]$ to $[0,1]$), and periodic Fourier series in z. The x-derivatives are approximated with modified Padé finite differencing due to Lele (1989). The nonlinear terms are evaluated in physical space. For the spectral directions (y and z) this requires FFT's to and from wave space. More collocation points are used in physical space than modes in wave space in order to control aliasing errors.

The equations are nondimensionalized by scaling with the half-thickness δ of the Gaussian mean inflow velocity profile and with the freestream velocity U_0. The Reynolds number based on these scales is defined by $Re = U_0\delta/\nu = 400$, and the inflow profile by $\bar{U}(y) = 1-\lambda\exp(-.69315y^2)$, where $\lambda = 0.692$ is the velocity defect (corresponding to the experiments of Sato & Kuriki 1961). The other nondimensional parameter of the problem is the Schmidt number $Sc = \nu/D = 1$, where D is the diffusion coefficient of the passive scalar.

Dirichlet boundary conditions are specified for the velocity perturbation at the inflow. 2-D Rayleigh equation eigenfunction profiles at a frequency of 0.5 and an amplitude of 0.06 are used for the streamwise and vertical velocities (u and v). The maximum growth rate occurs at a frequency of 0.614, but the lower value was used to compensate for the viscous thickening of the wake downstream. For the 3-D simulation steady profiles for v and the spanwise velocity w are added at the inflow to produce streamwise vorticity:

$$\omega_1(x=0,y,z) = (.034/k)\left(2+k^2-4y^2\right)e^{-y^2}\sin(kz),$$

where $k = 2\pi/L_z$ is the spanwise wavenumber, and L_z is the spanwise domain length. It has been observed that in mixing layers the spanwise wavelength is about 2/3 of the streamwise wavelength, so by analogy we chose $L_z = 6$ for the present work. This yields a maximum streamwise vorticity of 0.10 at the inflow. At the exit plane, each velocity component is required to satisfy a "convective" outflow boundary condition of the form $\partial\psi/\partial t = -c\,\partial\psi/\partial x$, where $c = 0.9$ is the approximate speed of the large structures near the exit. At infinity, all perturbations are set to zero.

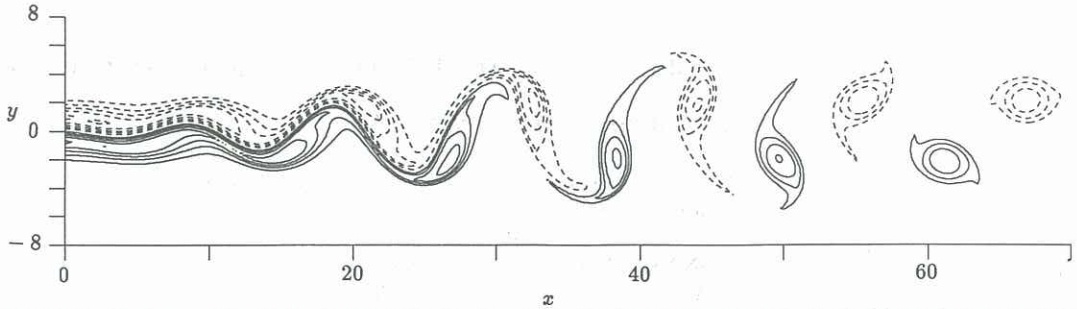

FIGURE 1. Contours of spanwise vorticity for the 2-D case. Contour interval is 0.1. Dashed lines denote negative levels, solid lines denote positive levels.

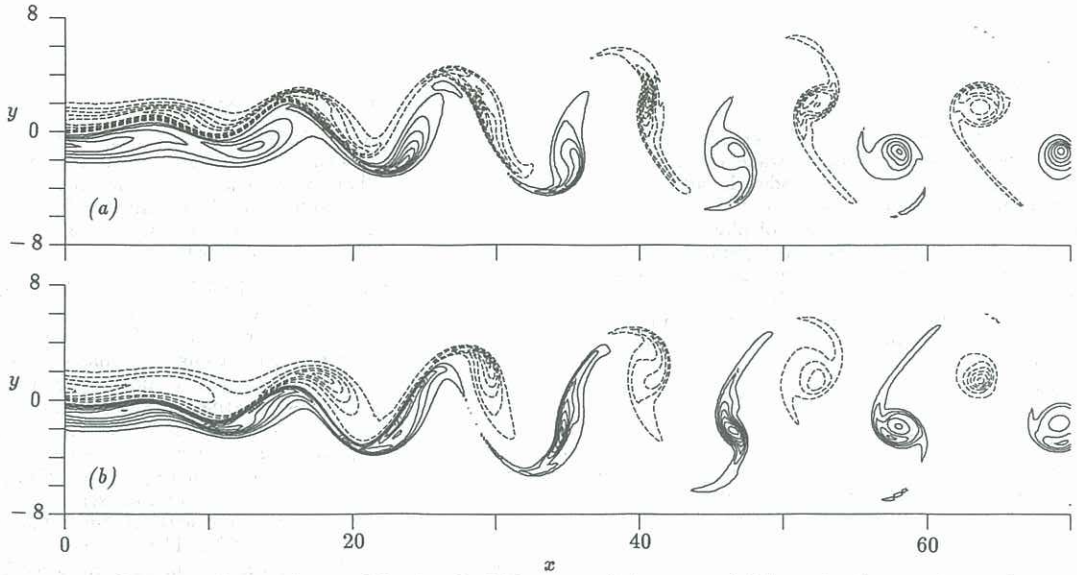

FIGURE 2. Contours of spanwise vorticity for the 3-D case at *(a)* $z = 0$ and *(b)* $z = 3$. Contour interval is 0.1.

The length of the computational domain is $L_z = 70$ and the vertical mapping parameter is $\beta = 6$. The mesh is $384 \times 128 \times 24$ (grid points in x, Fourier modes in y and z). Most of the aliasing errors were eliminated by using a collocation grid in the spectral directions of 160×32.

3. VORTICITY DYNAMICS

Shown in figure 1 are contours of spanwise vorticity (ω_3) for the base-line 2-D case. The formation of a vortex street consisting of alternating-sign vortices (rollers) is clearly seen. A consequence of conservation of angular momentum is the formation of "spiral arms" around each vortex; not all the vorticity can roll up into the vortex cores. Farther downstream these arms diffuse away, leaving nearly circular vortex cores. Note also the near-symmetry between the upper and lower vortices.

Contours of ω_3 for the 3-D case are plotted in figure 2 in the two x-y symmetry planes (where $\omega_1 = 0$). These planes are each between a pair of counter-rotating streamwise vortices. Qualitatively the same structures appear as in the 2-D case, but there are important quantitative differences. Considering the row of vortices along the top (negative ω_3), we see that the flow starts off very much like the 2-D flow, but by $x = 20$ significant distortion in z appears. At $z = 0$ the peak vorticity is on the inside edge of the rollers, while at $z = 3$ the peak vorticity is on the outside edge. This cannot be an advection effect since by $x \simeq 40$ the peak value of ω_3 reaches -0.8 (at the inflow it is about -0.5). Thus the variation in z must be due to vortex stretching effects. This enhancement of vorticity occurs at all z locations but is most pronounced at $z = 0$. Beyond $x \simeq 35$, a different process from the one responsible for the above enhancement becomes dominant. At $z = 3$, the maximum vorticity amplitude drops suddenly by $x = 40$, then rises to nearly its previous level by $x = 60$. At $z = 0$, a small, intense and nearly symmetric elliptic roller forms by $x = 40$. This is followed by a suppression of vorticity on one side of the center of the roller so that a nearly irrotational region is imbedded inside the roller by $x = 60$. Because of the symmetry in the inflow conditions, all of the above comments for the upper row of vortices at $z = 0$ and $z = 3$ apply to the mirror image in y of the lower row at $z = 3$ and $z = 0$, respectively.

Some of the mechanisms for the enhancement and suppression of ω_3 in certain regions are evident from an examination of the streamwise (ω_1) and vertical (ω_2) components of vorticity, shown in figure 3 at $z = 1.5$. Both components develop very quickly up to about $x = 25$, then decay slowly thereafter. At $z = 1.5$, ω_1 is positive at the inflow and leads directly to the formation of ribs with the same sign. These ribs can be divided into two sets; those with positive ω_2 and those with negative. For $x < 20$ the former are clearly associated with the upper rollers and the latter with the lower rollers. During the growth phase of the ribs, they connect spanwise vortices of like sign (see Chen *et al.* 1989).

In the early development of the wake, the ribs are intensified by the 2-D strain field of the main rollers (as in mixing layers), but this mechanism cannot increase the circulation around a rib. However, since the radius of the ribs remains about constant, the circulation increases significantly. The mechanism for this is the "conversion" of ω_3 into ω_1 by one of the "vortex stretching" terms of the ω_1 equation: $\partial\omega_1/\partial t = \ldots + (\partial u/\partial z)\omega_3 + \ldots$ The opposite-sign ω_1 near the rollers is due to the 3-D distortion of the rollers by the ribs and, as opposed to the ribs, does not see the large 2-D strain field caused by the rollers. In figure 2 note that the main effect of the 3-D distortion of ω_3 for $x < 35$ is the enhancement of vorticity along one side of a roller and suppression along the opposite side (both due to the vortex stretching terms produced by the ribs), thus shifting the peak vorticity towards one side. In the z-plane on the other side of a particular streamwise vortex,

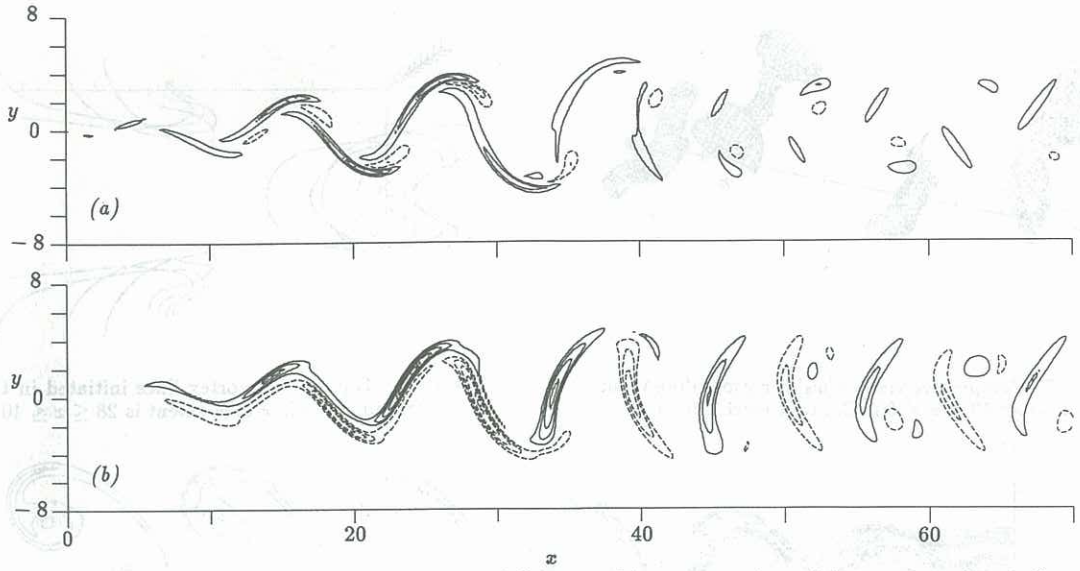

FIGURE 3. Contours of *(a)* streamwise vorticity and *(b)* vertical (cross-stream) vorticity corresponding to figure 2 at $z = 1.5$ Contour interval is 0.1.

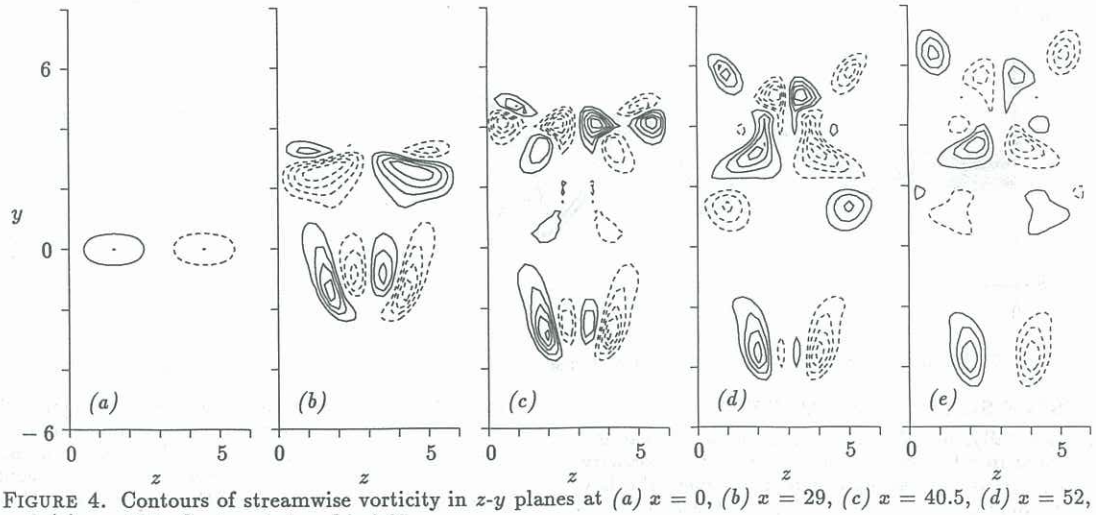

FIGURE 4. Contours of streamwise vorticity in z-y planes at *(a)* $x = 0$, *(b)* $x = 29$, *(c)* $x = 40.5$, *(d)* $x = 52$, and *(e)* $x = 63.5$. Contour interval is 0.05.

the peak vorticity is shifted to the other side of the same spanwise roller. Due to this distortion, the vortex lines in the rollers will have an x (as well as a y) component. Farther downstream, one end of each rib becomes increasingly associated with a roller on the opposite side of the wake. Also, they tend to stand nearly vertical, in contrast to a typical rib angle of 45° for $x < 25$ and for mixing layers. This transition coincides with the end of the growth of the ribs and the beginning of their decay.

Shown in figure 4 are spanwise (z-y) cuts of ω_1 at five x locations. The first plot shows the inflow forcing, and the others show cuts through the upper rollers. Note that in either half of the domain (*e.g.*, $0 \leq z \leq 3$), the magnitudes of the positive and negative streamwise vorticity are about the same even though there is only one sign at the inflow. For $x < 40$ the ribs (the lowest and highest pairs of vortices in figures 4(*b*-*e*)) have the characteristic shape of "non-collapsed" vortices – elliptical and tilted from the horizontal (see Lin & Corcos 1984). This is a relatively stable state. Farther downstream they begin to show signs of collapse to small, round and more intense vortices (however, a higher Reynolds number is needed to see this clearly). Comparing figures 2(*a*) and 2(*b*) at $x = 29$ to figure 4(*b*) we note that the regions of enhanced ω_3 are located in the middle of positive strain regions created by ω_1-quadrapoles. Similarly, regions of ω_3 suppression are also located in the middle of quadrapoles, but where the strain is negative. Further, half of the ω_1 vorticity involved is associated with ribs while the other half is due to the distortion of the rollers. By $x = 40$ (figure 4(*c*)), several changes in the structure of the flow have occurred. The ribs and rollers have moved away from one another so that the former are not a part of one of the above-mentioned quadrapoles and do not appear to significantly contribute to the strain in the vicinity of the rollers. Instead, new ω_1 is created within the rollers, which are then strained in a different manner than before. One can follow the evolution of ω_1 and see that the quadrapoles it forms are responsible for the changing distribution and intensity of ω_3.

A perspective view (figure 5) of the rollers located between $x = 40$ and $x = 60$ shows part of the evolution of ω_3. In figure 6 two perspective views of vortex lines initiated in the ribs located at $x = 28$ and $x = 34$ show the formation of vortex loops. Since both signs of ω_3 are needed to close the loops, the ribs must connect opposite-signed vortices. Farther upstream, vortex lines continue all the way across the span and are not closed, suggesting the ribs connect vortices of like sign. We note also that the vortex loops originally associated with the bottom half of the wake (one of which is shown at the left in the plots of figure 6) are all lined up and centered at $z = 3$ while the upper ones are centered at $z = 0$ (or, equivalently, $z = 6$). Introducing time-periodicity into ω_1 at the inflow will create other patterns of loops.

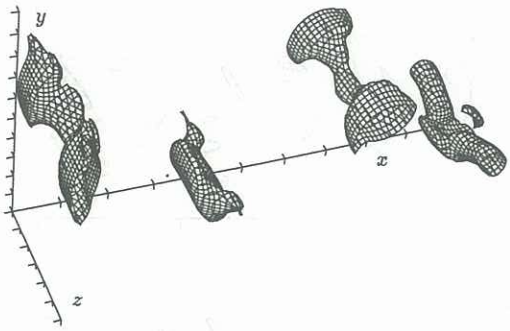

FIGURE 5. Perspective view of $|\omega_3|$ corresponding to figure 2 in the range $40 \leq x \leq 60$. Contour level is 0.35.

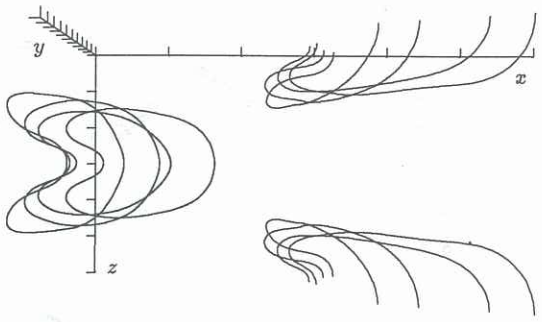

FIGURE 6. Top view of vortex lines initiated in the ribs at $x = 28$ and $x = 34$. x axis extent is $28 \leq x \leq 40$.

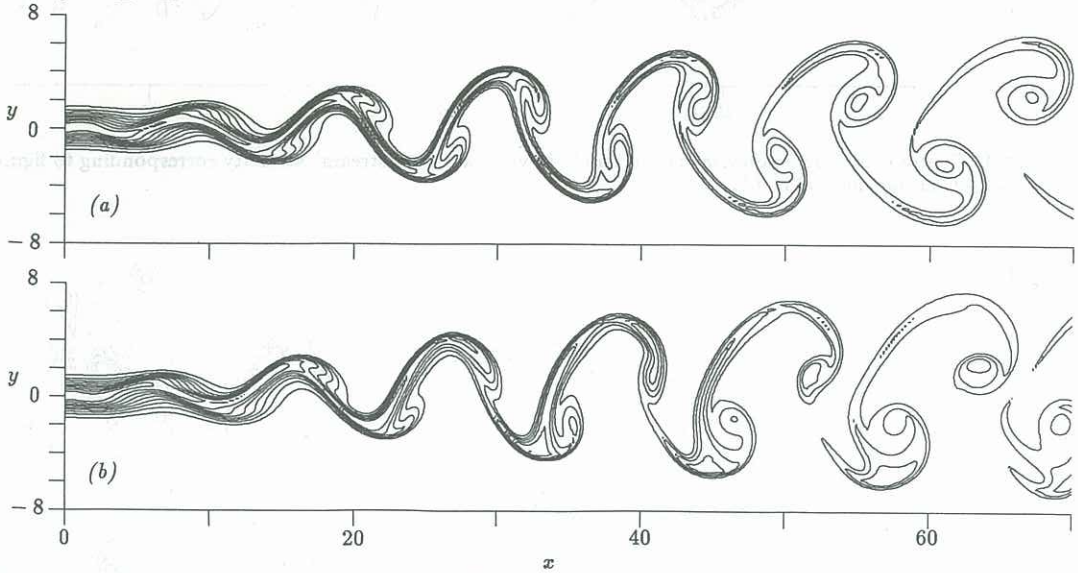

FIGURE 7. Passive scalar contours for the *(a)* 2-D case, and *(b)* 3-D case at $z = 0$. Contour interval is 0.1.

4. PASSIVE SCALAR CONVECTION

Experimentally, one often introduces smoke or heat as a passive scalar into the wake in order to trace the vorticity. Of course, this is only an approximation unless the flow is 2-D, the Schmidt number is unity, and the inflow passive scalar profile is identical to the vorticity profile. We tested this approximation here for both the 2-D and 3-D cases, using a Gaussian profile (with half-width 0.833) to model the injection of a passive scalar. Shown in figure 7 are the results for the 2-D case and for the 3-D case at $z = 0$. Comparing figures 1 and 7(*a*) we see significant differences. However, for $x > 45$, the maxima of the passive scalar lie very close to the extrema in vorticity, but with no consistent relative offset. For the 3-D case, a comparison of figures 2(*a*) and 7(*b*) shows larger differences. In particular, the upper and lower sides are less similar in the passive scalar than in the vorticity. Also, while there is a local maxima in the passive scalar near each roller, there are also concentrations of scalar in nearly irrotational areas as well. This may be an indication of history effects; the passive scalar may concentrate in regions of high vorticity, and then be left behind as the vorticity moves elsewhere through vortex-stretching effects.

5. SUMMARY

The calculations presented here show that in the very early stages of the development of a wake, the flow on each side is very similar to a mixing layer. Ribs form between rollers of like sign and are amplified. These ribs induce opposite-sign streamwise vorticity in the rollers which combine with the ribs to form quadrapoles of ω_1. The resulting strain region at the center of the quadrapoles either suppresses or amplifies (depending on z) the spanwise vorticity in the rollers. Farther downstream, mixing layer characteristics are replaced with wake characteristics. The ribs now connect rollers of opposite sign and start to decay. The distortion of the rollers produces new regions of streamwise vorticity which form quadrapoles different from before. Thus certain regions of ω_3 that were suppressed before are now amplified, and vice-versa. If this continues, this will lead to "blinking" of the rollers, although we emphasize that the computational box was only long enough to observe one cycle.

In two dimensions, it appears that a Gaussian profile for a passive scalar at the inflow produces a scalar field that correlates well with the vorticity. However, in 3-D the vortex stretching terms of the momentum equations distort the vorticity field so that while there are still extrema of ω_3 near the passive scalar maxima, the correlation is not as good as in 2-D.

REFERENCES

BUELL, J. C. 1989 A hybrid numerical method for three-dimensional spatially-developing free-shear flows, submitted to *J. Comp. Phys.*

CHEN, J. H., CANTWELL, B. J. & MANSOUR, N. N. 1989 AIAA Paper No. 89-0285, Reno.

LELE, S. K. 1988 private communication.

LIN, S. J. & CORCOS, G. M. 1984 *J. Fluid Mech.* **141**, 139–178.

MEIBURG, E. & LASHERAS, J. C. 1988 *J. Fluid Mech.* **190**, 1–37.

RILEY, J. J. & METCALFE, R. W. 1980 Direct numerical simulations of the turbulent wake of an axisymmetric body. *Turbulent Shear Flows 2,* 78–97.

SATO, H. & KURIKI, K. 1961 *J. Fluid Mech.* **11**, 321–352.

WRAY, A. A. 1989 Minimal storage time-advancement schemes for spectral methods, submitted to *J. Comp. Phys.*